Check for updates

New frontiers in intracranial imaging with HF-OCT: *Ex vivo* human cerebrovasculature evaluation and *in vivo* intracranial arteries dynamic visualization

Vania Anagnostakou[1], Mark Epshtein[1], Ahmet Peker[1], Ajit S. Puri[1], Jasmeet Singh[1], Giovanni J. Ughi[1,2] and Matthew J. Gounis[1]*

[1]New England Center for Stroke Research, Department of Radiology, University of Massachusetts Chan Medical School, Worcester, MA, United States, [2]Advanced Development Department, Gentuity, LLC, Sudbury, MA, United States

Optical coherence tomography (OCT) technology is a well-established diagnostic tool in multiple fields of medicine. Intravascular OCT has been used for more than a decade for the clinical imaging of coronary arteries, however, its use for the imaging of the human cerebrovasculature has been delayed by the challenges posed by the elevated vascular tortuosity. A novel high-frequency OCT (HF-OCT) probe designed for neurovascular use was evaluated in tortuous, *ex vivo*, human intracranial anatomy and, using an *in vivo* canine model, for the dynamic imaging of intracranial arteries and the subarachnoid trabecula (SAT). Using four cadavers, we investigated HF-OCT probe navigation and imaging performances in human anterior arterial circulation (from the M4 segment to internal carotid artery), in the posterior arterial circulation (from the P4 segment to vertebrobasilar junction) and in a broad range of venous sinuses. HF-OCT was able to gain distal access through elevated tortuosity and generate high-quality imaging data depicting vessel morphology, the vessel wall pathology (e.g., atherosclerotic disease and dissecting lesions), and the subarachnoid trabecula (SAT). Using an *in vivo* canine model, the HF-OCT probe was used to record stationary dynamic data in multiple intracranial vascular locations. Data showed the motion of the arteries and the SAT, including collisions between vessels, membranes, and the interaction between the SAT and the blood vessels. HF-OCT data allowed for the quantification of the dynamics of the vessels and the SAT, including vessel lateral motion with respect to the parenchyma, and collisions between large and small arteries. Results showed that the HF-OCT probe can overcome delivery obstacles in tortuous cerebrovascular anatomy and provide high-quality and high-resolution imaging at multiple distal locations, including M4 and P4 segments of the anterior and posterior circulations. HF-OCT has the potential to facilitate a better understanding of fine anatomical details of the cerebrovascular and perivascular environment, neurovascular disease, and collect real time information about the dynamics of the subarachnoid space and arteries and become a valuable diagnostic tool.

Introduction

Optical coherence tomography (OCT) is an imaging technique able to visualize tissue microstructure using low coherence lasers and interferometry techniques by measuring depth-resolved reflections of near-infrared light (Izatt et al., 1997; Xu et al., 2008; Tearney et al., 2012). This technology was originally developed for non-invasive imaging of biological tissue and initially commercialized for ophthalmic applications (Huang et al., 1991; Kim et al., 2015). One of the earlier clinical applications of OCT was the visualization of the peripapillary region of the retina and is now routinely used for diagnosis of retinal diseases and choroidal vasculature (Ploner et al., 2016). It is adopted in other areas like cardiology and routinely used for the imaging of coronary arteries and the optimization of percutaneous interventions (Prati et al., 2010; Koskinas et al., 2016; Ughi et al., 2016; Shlofmitz et al., 2018; Ali et al., 2021; Araki et al., 2022). Intravascular OCT has the ability to depict vessel wall characteristics not seen by other modalities due to an increased spatial resolution reaching the micrometer scale, producing images comparable to histology (Tearney et al., 1997). The applications of this technology have lately been explored in the neurovascular space and showed enormous potential (King et al., 2019; Caroff et al., 2020; Vardar et al., 2020). High-frequency OCT (HF-OCT) is a new generation modality, with a catheter technology developed specifically for neurovascular applications (Gounis et al., 2018; Ughi et al., 2020). In this study, we hypothesized that the HF-OCT catheter will be able to reach distal intracranial locations using standard angiographic techniques and acquire detailed images of the vessels and the perivascular environment. Here, we present its use for the *ex-vivo* investigation of human intracranial vasculature in cadavers in both the arterial and venous system, along with dynamic *in vivo* imaging of intracranial arteries in a preclinical model.

Materials and methods

High-Frequency optical coherence tomography neurovascular imaging technology

The HF-OCT probe prototype used in this study was developed for intracranial use (Ughi et al., 2020). Existing intravascular imaging solutions (e.g., OCT and IVUS) suffer from major limitations precluding their use in distal, tortuous, intracranial anatomies (Lopes and Johnson, 2012; Gounis et al., 2018). Neurovascular imaging probes have several requirements, including: reduced size for compatibility with neurovascular

access catheters; enhanced flexibility for navigation in highly tortuous vasculature; reliable image quality in highly tortuous vasculature free of distortions and other artifacts (Gounis et al., 2018). The HF-OCT probe has a maximum diameter of approximately 0.40 mm at the level of the joints and a diameter of approximately 0.36 mm for its entire length. It is made by nitinol material and the distal portion was designed to have a stiffness transition profile optimized to navigate elevated vascular tortuosity conditions. The distal end of the device includes a short transparent imaging window and a flexible, atraumatic spring tip, with significantly reduced stiffness compared to rapid exchange tips used by other intravascular imaging devices. A rotating optical element comprising of an 80-micron fiber and a ~1 mm long GRIN lens is encapsulated within the imaging window and the nitinol tube. The HF-OCT technology replaced the need of torque cables used by traditional intravascular imaging solutions (current OCT and IVUS) with a distal control element (Ughi et al., 2020). This solution adopts the use of an optically transparent viscous gel. Instead of a torque cable, the optical fiber itself is used to transmit the rotational torque between the system and the imaging lens, and the gel is used to distally control and ensure a constant rotation of the lens. This has significant advantages, including a reduced diameter size and enhanced rotational performances in tortuous conditions. It has been previously shown that this solution can acquire high-quality images free of non-uniform rotational distortion (NURD) artifacts in extremely tortuosity conditions (Ughi et al., 2020), which is further evaluated in this study in *ex vivo* human anatomy. The HF-OCT imaging console uses a swept source laser with a central wavelength of ~1300 nm that enables a scan range >6 mm (radius) and acquires data at a speed of 200 kHz (or 200,000 A-scan lines per second). Combined with the here presented HF-OCT neurovascular imaging probe, it acquires data at a speed of 250 Hz (or 250 images per second), with each individual HF-OCT cross-sectional image made by 800 A-scan lines to ensure an adequate number of samples at a distance of 6 mm.

Ex-vivo assessment of the human intracranial vasculature

We investigated the arterial and venous vasculature of human cadavers ($n = 4$) with the use of HF-OCT. In three of the cadavers, the arterial tree was imaged. The fourth cadaver was used for imaging of the venous system only. Lightly embalmed fresh frozen cadavers were used for the purposes of this study. Cannulas inserted into the right common carotid artery (CCA) and jugular vein were used to manually flush and remove blood products and clots.
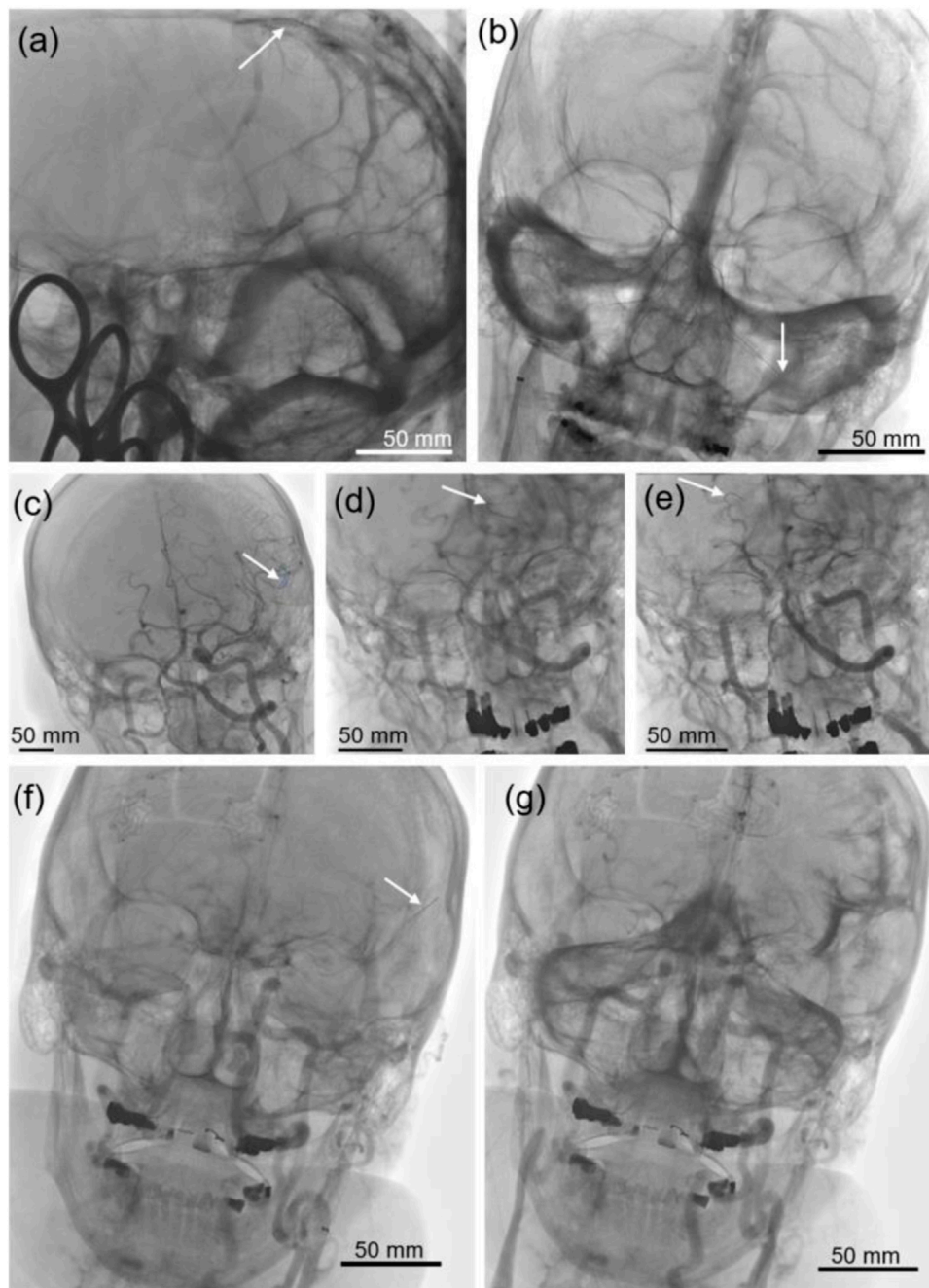
FIGURE 1
Fluoroscopic images of the venous sinuses and arteries. **(A)** The position of the optical coherence tomography (OCT) probe can be seen inside the superior sagittal sinus, and **(B)** along the course of the right inferior petrosal sinus (RIPS) through the cavernous sinus and into the left inferior petrosal sinus (LIPS). **(C,F)** The distal end of the OCT probe is advanced into the distal branches of the left middle cerebral artery (LMCA), and **(D)** inside the distal left and **(E)** the right posterior cerebral artery (PCA). **(G)** Contrast distribution inside the subarachnoid space after perforation of a distal LMCA branch.

For arterial access, the right femoral artery was surgical exposed and, under fluoroscopic guidance, an 8F wide and 45 cm long sheath was inserted using Seldinger technique followed by a long 6F sheath. For the anterior circulation, a single or double curved diagnostic catheter was used to select the left CCA and the internal carotid artery (ICA). The 6F was consecutively advanced over the catheter. Once access to the ICA was achieved, a Catalyst 5F distal access catheter (Stryker

Neurovascular, Fremont CA) was navigated with the help of a Synchro-14 guidewire (Stryker Neurovascular) and an SL-10 microcatheter (Stryker Neurovascular) deployed into the cavernous segment of the ICA. For the posterior circulation, the 6F long sheath was placed in the left or right vertebral artery, and a Catalyst 5F was advanced up to the vertebrobasilar junction or basilar artery.

In the anterior circulation, the microcatheter was navigated through the different branches of the superior and inferior divisions, and into multiple segments of the left middle cerebral artery (LMCA). At each location, the HF-OCT-catheter was delivered through the microcatheter. The microcatheter was then unsheathed to the most proximal location, and multiple pullbacks were performed covering locations from the M4 segment to the ICA. For the posterior circulation, the microcatheter was navigated through the left or right posterior cerebral artery (PCA) up to the P4 segment. Similarly to the anterior circulation, the HF-OCT-catheter was delivered, and multiple pullbacks were performed covering locations from the P4-segments to the vertebrobasilar junction. In one case, an intentional perforation of the M4-branch of the LMCA was accomplished with the microcatheter and microwire. Contrast was injected directly into the subarachnoid space (SAS) to inflate it and create a better environment for the near-infrared light to generate diagnostic quality HF-OCT images of the areas surrounding the vessels. Fluoroscopy was used to monitor contrast flow into the different compartments of the SAS.

For venous access, the right femoral vein was used. Using the same set-up, the 6F long sheath was positioned inside the right jugular vein and the 5F Catalyst was advanced either inside the superior sagittal sinus (for imaging of the sinus) or at the origin of the inferior petrosal sinus (IPS). For the superior sagittal sinus, an SL-10 microcatheter and Synchro-14 microwire were used and navigated up to the most distal segment of the sinus. For the IPS, the microcatheter was navigated into the right IPS through the cavernous sinus, then into the left IPS and left jugular vein. The OCT-catheter was delivered for each location through the microcatheter. Multiple pullbacks were performed in the different venous channels.

Pullbacks were acquired with the use of contrast media (Omnipaque 240) to facilitate clot removal from the segments undergoing imaging. A pump was used to inject contrast during pullbacks to enhance clearance of the vessel lumen from residual clots (Figure 1).

In-vivo dynamic imaging of the subarachnoid space in an animal model

Imaging of the subarachnoid space was performed in a canine model *in vivo*. Using standard protocols, the animal was intubated and put under general anesthesia. After surgical

exposure of the femoral artery, the vertebrobasilar system of the animal was accessed with our standard technique as described in our previous work (Anagnostakou et al., 2022). Specific HF-OCT acquisitions were performed to investigate the architectonics of the subarachnoid space, the density and configuration of arachnoid membranes, the subarachnoid trabeculae (SAT) surrounding the basilar artery, and the anterior spinal artery as described in our previous experimental work (Anagnostakou et al., 2022). Dynamic imaging was performed close to the craniocervical junction and cervical level, where multiple membranes connecting to dominant vessels were seen. The imaging lens of the OCT probe was positioned intravascularly at the chosen location, and a stationary acquisition performed for 3 s with and without breath-hold while injecting contrast media at 3.5 ml/s.

Data analysis and image processing

The *ex-vivo* pullbacks were aligned and explored for recognizable patterns. To generate 3D renderings, the pullbacks were denoised, segmented, and reassembled in red-green-blue (RGB) by removing the interior of the vessel, as previously described (Anagnostakou et al., 2022). The stationary HF-OCT acquisitions were taken for 3 s at a rate of 250 frames/sec. Analysis was done every 10 slices. By positioning markers on objects that could be recognized across all the slices, we were able to calculate the kinematics of the arteries, and some of the SAT (see Supplementary Material for detailed description, equations, and code) as well as qualitatively describe their motion.

To determine the relative velocity of the arteries, the components of the relative velocity were calculated, and intensity obtained (Eq. 1). The relative velocity components were obtained as the derivative of the position vectors for each axis for each of the objects and the subtracting them (Eq. 2 where x_1, x_2, y_1, y_2 are position vectors for each of the objects).

$$V_{rel} = \sqrt{V_{rel_x}^2 + V_{rel_y}^2} \qquad (1)$$

$$V_{relx} = \frac{dx_2}{dt} - \frac{dx_1}{dt}, V_{rel_y} = \frac{dy_2}{dt} - \frac{dy_1}{dt} \qquad (2)$$

Results

Ex-vivo intracranial imaging

We performed a total of 18 pullback acquisitions from the anterior ($n = 10$) and posterior arterial circulation ($n = 8$) of 3 different cadavers (2 males and 1 female, age ranged between 59 and 75 years). A fourth cadaver was used for imaging of
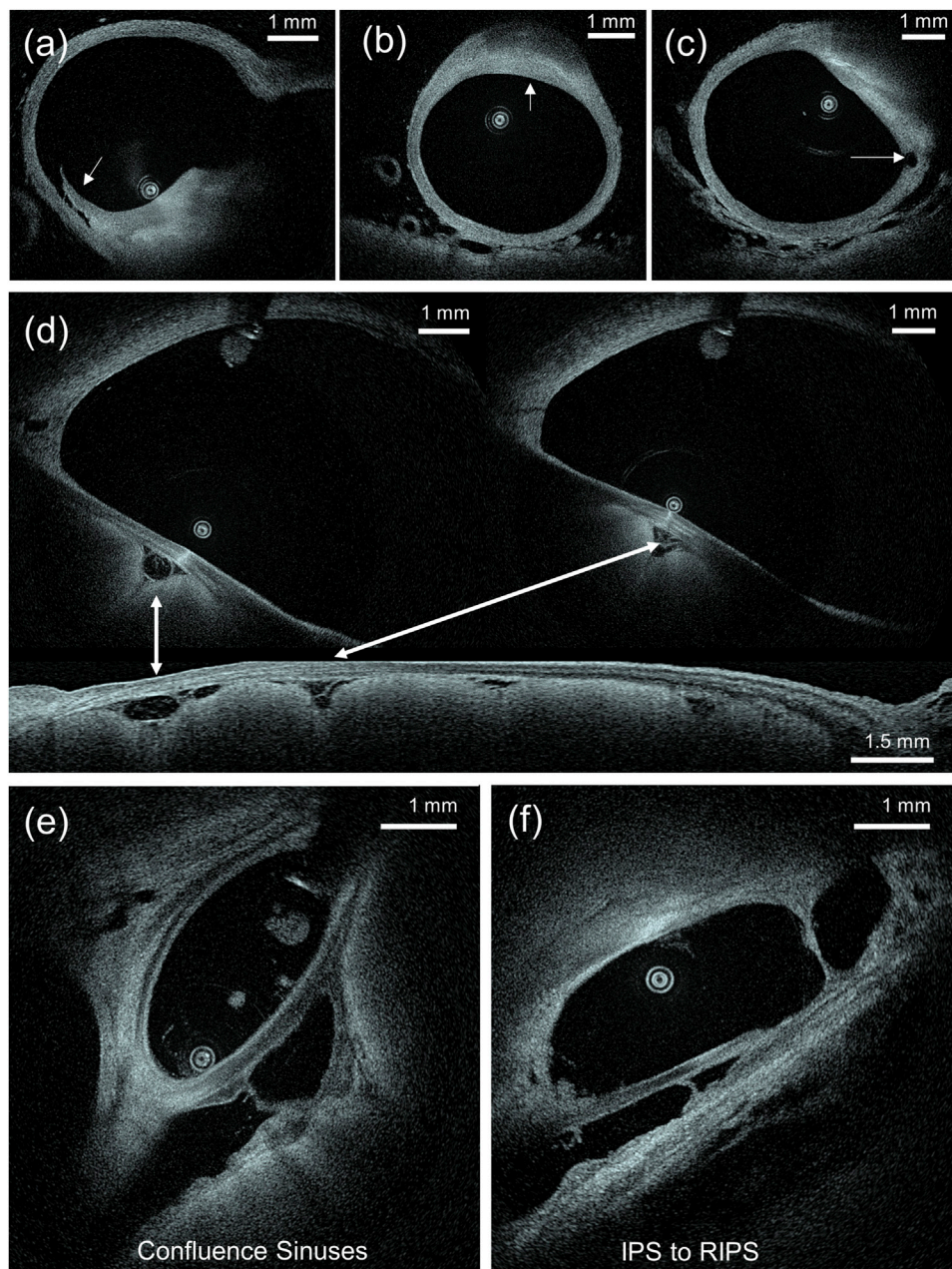
FIGURE 2
(A−C) Examples of atherosclerotic plaque morphology of the wall of the basilar artery. Figure **(A)** shows a dissecting flap on the shoulder of a thick fibrotic cap can be identified. Figure **(B)** shows a focal, lipid core, fibroatheroma. In figure **(C)**, a small perforating vessel arising from a lipid plaque (right side) can be seen. **(D)** Axial and sagittal view of the sigmoid sinus where vessels inside the subarachnoid space are observed between the sinus and the brain parenchyma. **(E)** Image at the level of the confluence of sinus where multiple venous channels meet, and **(F)** inside the IPS where more than one channels are visible.

venous channels. The left ICA was used to access the anterior circulation in all cases. For the posterior circulation, both vertebral arteries were used. Multiple acquisitions were obtained to ensure the reproducibility of the OCT probe navigation in multiple intracranial vessels and vascular

territories. Various levels of difficulty were found in accessing vasculature using standard neurovascular devices. Regardless of access challenges, in all cases, the HF-OCT probe was able to reach with ease and image all locations that were reached with a microcatheter. Three (3) pullbacks of the anterior circulation
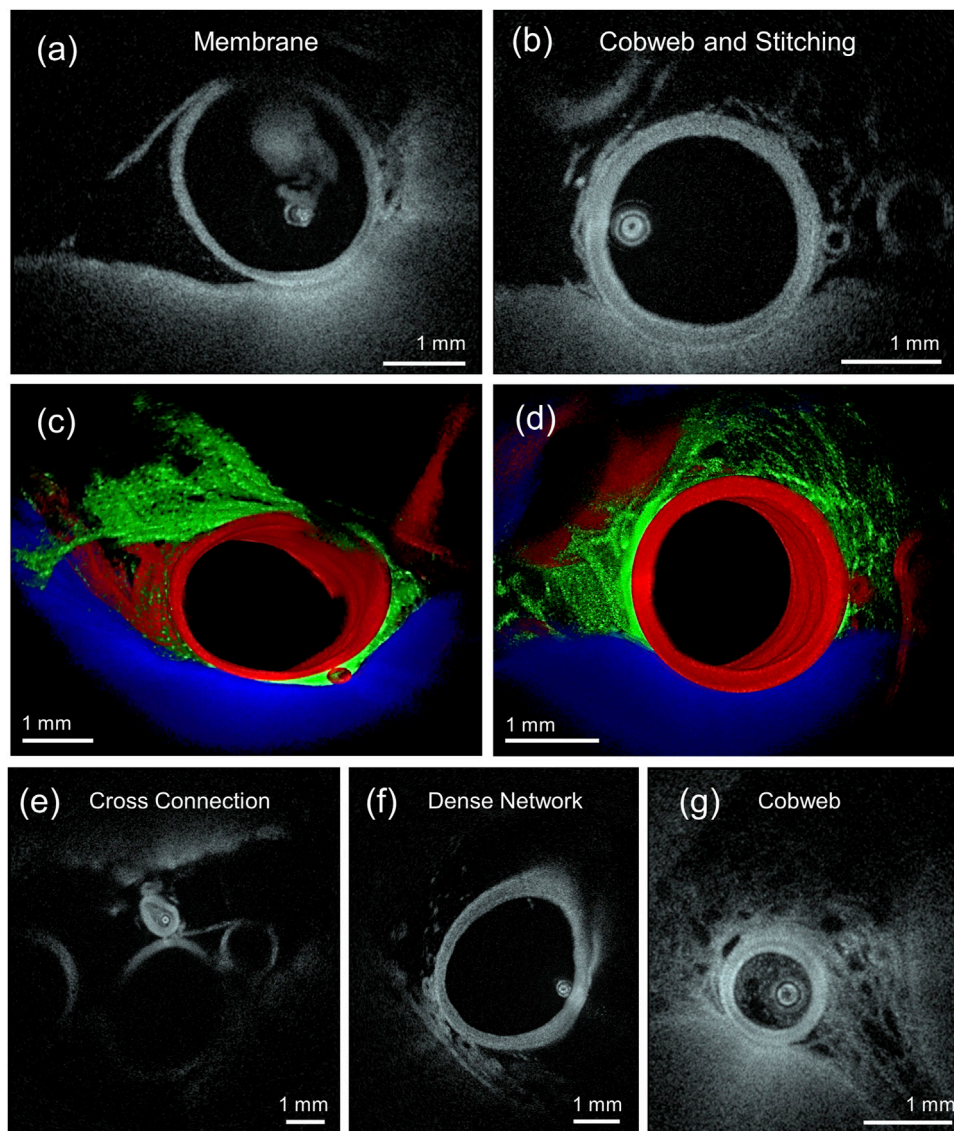
FIGURE 3
(A,C) HF-OCT imaging depicting a subarachnoid membrane covering an artery and **(B,D)** a cobweb type subarachnoid trabeculae (SAT) on the right, with stitching fibers between the middle and upper left arteries. The three-dimensional (3D) renderings are obtained by segmenting and depicting the artery in red, SAT in green, and the parenchyma in blue. **(E)** HF-OCT cross-sectional slice depicting a cross connection type SAT between two arteries. **(F)** Slice depicting a dense network type SAT, and **(G)** a slice depicting a cobweb type SAT.

were performed with contrast injections directly into the subarachnoid space, and one from within the space. In six pullbacks unsatisfactory clot flushing obscured image quality. Although the HF-OCT system used in this study offers the synchronized acquisition of HF-OCT along with angiography, this feature was not adopted in this study. As such, the anatomical levels could only approximately be determined, the exact location of the optical lens and exact length of the vessel segment imaged could not be established accurately. Injection of contrast from a sulcal area adjacent to an M4 branch of the

LMCA resulted in contrast partially filling the subarachnoid space of the unilateral hemisphere and posterior fossa.

In all pullbacks (n = 18), branching points and perforators were recognized in fine details. In areas where the field of view of the HF-OCT system prototype was wide enough for the specific location (~13.8 mm in diameter), the parenchyma was also recognized surrounding vessels, perforators, and membranes. By examining the collected images, in one case, multiple eccentric thickening locations of the vessel wall were observed, without any significant stenosis of the lumen. Loss of normal

layering of the vessel wall was visible in both anterior and posterior circulation vessels, a presentation compatible with diffuse atherosclerosis (Figure 2). Lesions were more prominent along the basilar artery, the proximal segments of the MCA, and in the ICA. The exact extent of the atherosclerotic lesions was evaluated slice by slice, until normal or almost normal vessel wall re-appeared. The relationship between the plaque and adjacent branches, orifice involvement, and exact locations of wall thickening were seen in detail along with imaging features of plaque morphology and other characteristics, such as intimal thickening and presence of fibrotic, lipid core plaques (Figures 2A,C). Pullbacks performed in the venous channels revealed another range of findings. Venous sinuses were visualized fully or partially, with most of them traveling inside or adjacent to bony structures (Figures 2E,F). Veins of varied sizes were observed entering larger sinuses and at the level of the superior sagittal sinus, and the relationship to the brain parenchyma accurately depicted (Figure 2D).

The higher spatial resolution of HF-OCT and the favorable, transparent optical properties of the cerebrovascular fluid (CSF) allowed for imaging of the various elements of the perivascular space. Arachnoid membranes and subarachnoid trabeculae (SAT), along with their relationship to the arteries and adjacent parenchyma, were recognized. Variability in morphology and density was observed between cadavers and locations. In one cadaver, membrane rich areas were recognized along the M4-and M3-segment of the MCA, and the P4- and P3-segment of the PCA. The proximal basilar artery showed minimal amount of SAT and trabeculae. Distinct configurations of arachnoid membranes connecting to neighboring structures were identified and categorized as cobweb (Figure 3), where a multi-fenestrated, continuous membranous structure is present, trabecular stitching with fine fibers connecting between different vessels, and SAT networks of different densities (Figure 3F) (Anagnostakou et al., 2022). Multiple SAT were recognized surrounding perforators arising from the MCA.

In-vivo imaging

We performed dynamic acquisitions ($n = 6$) in two separate animals, with ($n = 2$) and without ($n = 4$) breath hold. The selected levels of imaging at the craniocervical and cervical planes showed subarachnoid membranes connecting to each other and to the vessels present at specific locations. Sequential imaging was performed while the vessels and surrounding structures contracted and relaxed following hemodynamic parameters of the cardiac cycle. Movement of the spine parenchyma, vessel wall, and membranes were recorded during 5 or 6 cardiac cycles per pullback. Relative movement of vessels towards and from the parenchyma and bony structures was seen along with a fine oscillation of subarachnoid membranes. Structures located adjacent to the spinal artery exhibited oscillatory movements that followed the cardiac cycle during systole and diastole. As a result, vessels, membranes, and parenchyma moved away or towards each other depending on the timepoint of the cardiac cycle. Membranes specifically exhibited a high degree of deformation showing sudden tension in the systole that interacts with the lateral motion of the artery and collapse with creasing during diastole. Furthermore, the membranes appeared to be loaded differentially, while one part of the membrane was under tension, and another was wrinkling under compression (Supplementary Video S1 and Figures 4A,B). The artery showed position changes up to 30% from diastole to systole, with respect to a given point on the parenchyma (Figure 4C). We also observed a relative motion between larger and smaller arteries, resulting in periodic collisions at speeds up to ~3 mm/s (Figure 4G and Supplementary Video S2). A qualitative visual comparison between imaging with and without breath hold did not reveal any substantial differences. However, when measured, the relative motion of the cross-connecting membrane attachment points to the proximal basilar bifurcation showed up to 14% difference between systole and diastole with breath hold, under 10% without, and both in rhythm with the heartbeat. However, during a breath hold, the elongation reached a periodic plateau; without breath hold, there was none (Figure 4H and Supplementary Video S3). Finally, we were able to visualize movement on miniature particulate motion within the CSF as can be seen in Supplementary Video S4.

Discussion

In this study, we demonstrated the feasibility of a novel neurovascular HF-OCT catheter to navigate human intracranial vasculature and depict anatomical and pathological features of the vessel wall and the perivascular environment *ex vivo*. To our knowledge, this is the first transfemoral successful navigation of an imaging catheter into the tortuous human intracranial vasculature reaching the most distal segments of both anterior and posterior circulations and able to produce high-quality, high-resolution images. Furthermore, intravenous images from a variety of cerebral sinus were similarly acquired. Contrary to the failure of initial studies evaluating the use of commercial coronary OCT systems (Lopes and Johnson, 2012), HF-OCT technology was dependably navigated beyond the carotid siphon and the basilar artery through extensive tortuosity, and as distally as the M4 and P4 segment of the MCA and PCA. Despite well-known challenges encountered during catheterization which were solely related to the specific anatomy and aged vessels of our cadavers, once the microcatheter deployment was achieved, the HF-OCT-probe placement and imaging did not present any additional difficulty. In all cases, the left ICA was used for navigation. This was chosen due to its known more
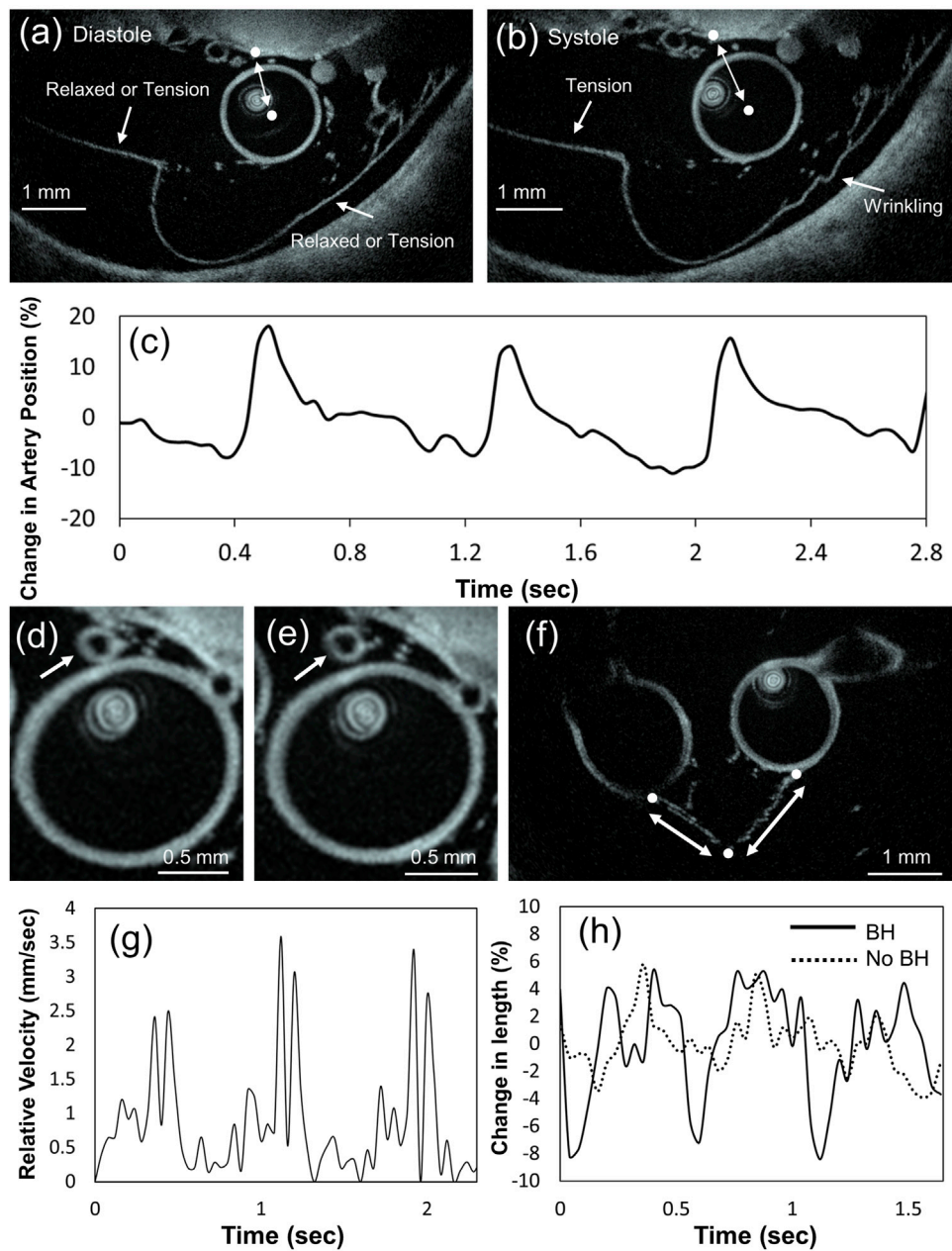
FIGURE 4
(A) Diastole: membrane is marked in two places, where it appears to be under tension or relaxed; the center of the artery and the parenchyma are marked by white points. During diastole they appear to be the closest to each other (Supplementary Video S1). **(B)** Systole: the membrane on the left is under tension, while on the right it is wrinkling under compression. The center of the artery and a point on the parenchyma (marked by white point) are now the most distant from each other (Supplementary Video S1). **(C)** Graph showing the change between the distance of the center of the artery and the chosen point on the parenchyma during heartbeat. The motion appears synchronized with the heartbeat. **(D,E)** Slices showing the collision of a small size artery with a larger artery (Supplementary Video S2). **(F)** Slice showing two arteries connected by cross connection type SAT: the attachment points to the arteries and the cross-connection point are marked by white dots; the extending fibers are marked by double arrows. **(G)** Graph showing the relative speed of the colliding arteries and **(H)** graph showing the change in distance between the points marked in figure **(F)**.

challenging access and catheterization when compared to the right, as the study aim was to evaluate navigation of the OCT device in the most challenging scenario. Taken together, this demonstrated the capabilities of HF-OCT to image intracranial

locations that are inaccessible to any other available intravascular imaging modality, such as conventional OCT and IVUS. Due a significantly higher spatial and temporal resolution, HF-OCT could offer an enhanced guidance for endovascular stroke

interventions with respect to currently available non-invasive imaging technologies, such as digital-subtraction angiography and cone-beam CT. (Ughi et al., 2020).

Other investigators have performed OCT imaging in *ex vivo* humans with a transfemoral approach (Mathews et al., 2011), or *in vivo*, however, imaging was limited only to the vertebral arteries (Given et al., 2015) and the less tortuous cavernous segment of the ICA (Su et al., 2008). For the assessment of more distal territories *ex vivo*, previous studies were limited to explanted cerebral vessels of the circle of Willis (Hoffmann et al., 2016; Weigand et al., 2019). In this study, we collected images of the main branches of the MCA and branching points, as well as the basilar and the PCA, depicting a plethora of perforators not routinely seen on angiography. Perforators with a lumen diameter as low as ~100 μm were visualized, including their origin from the parent artery (e.g., basilar or MCA). HF-OCT provided excellent anatomical detail due to its high spatial resolution, with images comparable to histology (Ughi et al., 2014). In distal, smaller diameter vessel segments, the field of view allowed for imaging of adjacent vessels and subarachnoid structures, along with brain parenchyma, visualizing the relationship between vessel, parenchyma, and arachnoid membranes.

Guided by previous findings in an *in vivo* canine model (Anagnostakou et al., 2022), where the architectonics of the subarachnoid space were studied, in this *ex vivo* model we expanded the imaging and characterization of the subarachnoid trabeculae (SAT) and membranes in other specific anatomical locations. Different SAT configurations were observed. Those were similar to our preclinical canine model, however, due to the small sample size of this study, a statistical assessment of location specific types of SAT was not performed. We nonetheless observed significant variability in membrane morphology amongst the three cadavers. The random orientation of the trabecular fibers that remain after completion of the embryological process of SAS development (McLone and Bondareff, 1975) might be partially responsible for this variability. Subarachnoid membranes and SAT are known to be collagen type I structures (Saboori and Sadegh, 2015) and, in the same way collagen fibers age elsewhere in the body with decrease of collagen fibers and collagen density (Van Gulick et al., 2019), aging and modification of collagen present in the SAS could possibly contribute to the variability in the elderly specimens we used.

Similar to cardiology, where OCT has been routinely used and has been able to precisely characterize plaques in the coronary arteries and detect intraluminal thrombus (Kubo et al., 2007; Johnson et al., 2019), intracranial atherosclerosis can also be evaluated with the use of OCT technology. Although only a few *ex vivo* (Mathews et al., 2011; Weigand et al., 2019) and *in vivo* (Given et al., 2015; Gao et al., 2018; Pasarikovski et al., 2019; Xu et al., 2020) studies were presented in the neurovascular space investigating intra-arterial luminal narrowing, there is

concrete evidence that HF-OCT is able to image and characterize intracranial plaques, features related to plaque instability, intraluminal thrombus formation, and their relationship to perforators as well as intracranial arterial dissections. In the examined cadavers, atherosclerotic plaques were found in multiple locations. HF-OCT depicted the location of the plaque inside the vessel wall and its extent, cap thickness, and degree of luminal narrowing and other imaging characteristics, such as tissue composition. Dissection flaps were also clearly visualized. Although in some segments of the acquired data sets image quality was reduced or diminished (either from inadequate cadaveric vessels distention due to unsatisfactory vessel pressurization or because of inadequate clot flushing), no failure, damage, or breakage of an OCT-probe occurred in these highly tortuous anatomies.

The larger diameter of venous sinuses compared to arteries did not allow for a complete visualization of the whole venous channel in certain specific areas. The location of the HF-OCT probe inside the sinuses influenced what was finally depicted on the image, and, when eccentric within the sinus, the field of view of the HF-OCT system was insufficient to visualize the whole venous channel. However, despite this limitation, the wall with overlying dura and bone could be seen, along with the presence of channels inside the IPS and multiple small veins entering the sinuses at different segments. No arachnoid granulations were seen inside the venous channels, possibly due to the lack of CSF flow and absence of pressure gradient *ex vivo*. A larger field-of-view can be accommodated by future improvements to HF-OCT technology, if required by clinical applications.

In the *in vivo* canine model, using the OCT probe to record stationary videos at a particular location, we were able for the first time to see live, in real time, the relative motion of the arteries, parenchyma, and SAT membranes. A significant lateral motion of arteries, as well as routine collisions between the vessels in normal operation was observed. The differential loading of the membranes, a result of being under tension and collapsing under compression (Figures 4A,B), are a possible consequence of the connections across the membranes which isolate parts from the applied load. However, these motions interact with CFS in a complex fluid–solid interaction, limiting the finding of this study to understand the dynamics of the SAT. All the videos were acquired while injecting contrast media at a constant rate. As such, injection could have played a role on the motion of the arteries, however, the motion of the vessels and the surrounding structures was found to be periodic with the heartbeat. This shows that if any external influence exists, it only introduces limited bias. Determining the precise nature of this motion is a promising avenue of research, but beyond the scope of this work.

Our findings indicate that intracranial OCT imaging could also have a role in the evaluation of CSF flow dynamics. If SAS can be seeded with suitable particles, velocimetry methods (Adrian and Westerweel, 2011) could be applied to visualize the flow of CSF in two dimensions, perpendicular to the artery

containing the probe. As a preliminary attempt, we visualized miniature particulate residue in the cadaver SAS where the CSF movement was caused by OCT-probe pullbacks and contrast injections. However, due to the random motion of the particles and limited signal-to-noise ratio, we were unable to produce meaningful flow streamlines (see Supplementary Material and Supplementary Video S4). Nevertheless, the ability to see particulate matter across multiple slices suggests that *in vivo* PIV of the CSF is possible.

Additional findings are that, at places such as the proximal basilar bifurcation, the SAT forming the cross connection significantly restrict the motion of the arteries. The plateau reached at their deformation suggests an apparent viscoelastic behavior, possibly one that stems not only form the material properties of collagen, but also from its shape and structure (Saboori, 2021). However, disappearance of the plateau without breath hold maybe be due to the introduction of another frequency to the motion which prevents the full extension of fibers, or the breath hold itself caused a slight rise in blood pressure which caused more pronounced motion in the arteries like it may happen in humans (Parkes et al., 2014). However, limited data collected in this study prevent further elucidation of this process. In other places such as the spinal artery, there seem to be significant lateral motion but with violent interaction with SAT and other arteries. Since brain aneurysms often interact with SAT (Gazi Yaşargil et al., 1976), we can hypothesize that the SAT themselves, collisions, and periodic tension at discrete attachment points may eventually cause or predispose the location for such injury or pathology (Mortazavi et al., 2018).

Further studies will be required to investigate these hypotheses in depth, however, findings from this study showed for the first time that intravascular OCT can be used to view the motion of extravascular structures *in situ*, which can potentially become a clinically relevant diagnostic tool. In particular, investigating the change in motion of certain arteries may indicate changes in elasticity and the onset of atherosclerosis (Boesen et al., 2015) as well visualizing active microbleeds in SAS and tears in SAT following head trauma which are not easily identified in pullbacks. Other uses may be discovered with routine use and the creativity and needs of practitioners.

Conclusion

OCT technology is a well-established imaging tool in multiple fields of medicine. In the neurovascular space, however, vascular access and delivery challenges due to the highly tortuous anatomy prevented its adoption in clinical practice. In the current study, we showed that a novel HF-OCT probe can overcome these delivery

obstacles and provide unparalleled, higher resolution imaging in tortuous intracranial anatomy. HF-OCT could facilitate a better understanding of fine details of the cerebral vasculature and perivascular environment, as well as providing real time information about the dynamics of the subarachnoid space and vessels.

Data availability statement

The raw data supporting the conclusions of this article will be made available by the authors, without undue reservation.

Ethics statement

The animal study was reviewed and approved by University of Massachusetts Medical School.

Author contributions

All authors read and edited the manuscript. VA, ME, and AP collected and analyzed the data.

Conflict of interest

Author GU was employed by the company Gentuity LLC.
The remaining authors declare that the research was conducted in the absence of any commercial or financial relationships that could be construed as a potential conflict of interest.

Publisher's note

All claims expressed in this article are solely those of the authors and do not necessarily represent those of their affiliated organizations, or those of the publisher, the editors and the reviewers. Any product that may be evaluated in this article, or claim that may be made by its manufacturer, is not guaranteed or endorsed by the publisher.

Supplementary material

The Supplementary Material for this article can be found online at: https://www.frontiersin.org/articles/10.3389/fphot.2022.988018/full#supplementary-material

References

Adrian, R. J., and Westerweel, J. (2011). *Particle image velocimetry*. Cambridge, United Kingdom: Cambridge University Press.

Ali, Z. A., Karimi Galougahi, K., Maehara, A., Shlofmitz, R. A., Fabbiocchi, F., Guagliumi, G., et al. (2021). Outcomes of optical coherence tomography compared with intravascular ultrasound and with angiography to guide coronary stent implantation: One-year results from the ilumien iii: Optimize pci trial. *EuroIntervention* 16, 1085–1091. doi:10.4244/eij-d-20-00498

Anagnostakou, V., Epshtein, M., Ughi, G. J., King, R. M., Valavanis, A., Puri, A. S., et al. (2022). Transvascular *in vivo* microscopy of the subarachnoid space. *J. Neurointerv. Surg.* 14, 420–428. doi:10.1136/neurintsurg-2021-018544

Araki, M., Park, S. J., Dauerman, H. L., Uemura, S., Kim, J. S., Di Mario, C., et al. (2022). Optical coherence tomography in coronary atherosclerosis assessment and intervention. *Nat. Rev. Cardiol.* doi:10.1038/s41569-022-00687-9

Boesen, M. E., Singh, D., Menon, B. K., and Frayne, R. (2015). A systematic literature review of the effect of carotid atherosclerosis on local vessel stiffness and elasticity. *Atherosclerosis* 243, 211–222. doi:10.1016/j.atherosclerosis.2015.09.008

Caroff, J., King, R. M., Ughi, G. J., Marosfoi, M., Langan, E. T., Raskett, C., et al. (2020). Longitudinal monitoring of flow-diverting stent tissue coverage after implant in a bifurcation model using neurovascular high-frequency optical coherence tomography. *Neurosurg.* 87, 1311–1319. doi:10.1093/neuros/nyaa208

Gao, P., Gui, L., Yang, B., Krings, T., and Jiao, L. (2018). Optical coherence tomography of spontaneous basilar artery dissection in a patient with acute ischemic stroke. *Front. Neurol.* 9, 858. doi:10.3389/fneur.2018.00858

Gazi Yaşargil, M., Kasdaglis, K., Jain, K. K., and Weber, H-P. (1976). Anatomical observations of the subarachnoid cisterns of the brain during surgery. *J. Neurosurg.* 44, 298–302. Available at: https://thejns.org/view/journals/j-neurosurg/0044/0023/article-p0298.xml. doi:10.3171/jns.1976.44.3.0298

Given, C. A., Ramsey, C. N., Attizzani, G. F., Jones, M. R., Brooks, W. H., Bezerra, H. G., et al. (2015). Optical coherence tomography of the intracranial vasculature and wingspan stent in a patient. *J. Neurointerv. Surg.* 7, e22. doi:10.1136/neurintsurg-2014-011114.rep

Gounis, M. J., Ughi, G. J., Marosfoi, M., Lopes, D. K., Fiorella, D., Bezerra, H. G., et al. (2018). Intravascular optical coherence tomography for neurointerventional surgery. *Stroke* 50, 218–223. doi:10.1161/strokeaha.118.022315

Hoffmann, T., Glaßer, S., Boese, A., Brandstädter, K., Kalinski, T., Beuing, O., et al. (2016). Experimental investigation of intravascular oct for imaging of intracranial aneurysms. *Int. J. Comput. Assist. Radiol. Surg.* 11, 231–241. doi:10.1007/s11548-015-1275-1

Huang, D., Swanson, E. A., Lin, C. P., Schuman, J. S., Stinson, W. G., Chang, W., et al. (1991). Optical coherence tomography. *Science* 254, 1178–1181. doi:10.1126/science.1957169

Izatt, J., Kulkarni, M. D., Kobayashi, K., Sivak, M. V., Barton, J. K., and Welch, A. J. (1997). Optical coherence tomography for biodiagnostics. *Opt. Photonics News* 8, 41. doi:10.1364/opn.8.5.000041

Johnson, T. W., Raber, L., di Mario, C., Bourantas, C., Jia, H., Mattesini, A., et al. (2019). Clinical use of intracoronary imaging. Part 2: Acute coronary syndromes, ambiguous coronary angiography findings, and guiding interventional decision-making: An expert consensus document of the european association of percutaneous cardiovascular interventions. *Eur. Heart J.* 40, 2566–2584. doi:10.1093/eurheartj/ehz332

Kim, J., Brown, W., Maher, J. R., Levinson, H., and Wax, A. (2015). Functional optical coherence tomography: Principles and progress. *Phys. Med. Biol.* 60, R211–R237. doi:10.1088/0031-9155/60/10/r211

King, R. M., Marosfoi, M., Caroff, J., Ughi, G. J., Groth, D. M., Gounis, M. J., et al. (2019). High frequency optical coherence tomography assessment of homogeneous neck coverage by intrasaccular devices predicts successful aneurysm occlusion. *J. Neurointerv. Surg.* 11, 1150–1154. doi:10.1136/neurintsurg-2019-014843

Koskinas, K. C., Ughi, G. J., Windecker, S., Tearney, G. J., and Raber, L. (2016). Intracoronary imaging of coronary atherosclerosis: Validation for diagnosis, prognosis and treatment. *Eur. Heart J.* 37, 524–535. doi:10.1093/eurheartj/ehv642

Kubo, T., Imanishi, T., Takarada, S., Kuroi, A., Ueno, S., Yamano, T., et al. (2007). Assessment of culprit lesion morphology in acute myocardial infarction: Ability of optical coherence tomography compared with intravascular ultrasound and coronary angioscopy. *J. Am. Coll. Cardiol.* 50, 933–939. doi:10.1016/j.jacc.2007.04.082

Lopes, D. K., and Johnson, A. K. (2012). Evaluation of cerebral artery perforators and the pipeline embolization device using optical coherence tomography. *J. Neurointerv. Surg.* 4, 291–294. doi:10.1136/neurintsurg-2011-010102

Mathews, M. S., Su, J., Heidari, E., Levy, E. I., Linskey, M. E., and Chen, Z. (2011). Neuroendovascular optical coherence tomography imaging and histological analysis. *Neurosurgery* 69, 430–439. doi:10.1227/neu.0b013e318212bcb4

McLone, D. G., and Bondareff, W. (1975). Developmental morphology of the subarachnoid space and contiguous structures in the mouse. *Am. J. Anat.* 142, 273–293. doi:10.1002/aja.1001420302

Mortazavi, M. M., Quadri, S. A., Khan, M. A., Gustin, A., Suriya, S. S., Hassanzadeh, T., et al. (2018). Subarachnoid trabeculae: A comprehensive review of their embryology, histology, morphology, and surgical significance. *World Neurosurg. x.* 111, 279–290. doi:10.1016/j.wneu.2017.12.041

Parkes, M. J., Green, S., Stevens, A. M., and Clutton-Brock, T. H. (2014). Assessing and ensuring patient safety during breath-holding for radiotherapy. *Br. J. Radiol.* 87, 20140454. doi:10.1259/bjr.20140454

Pasarikovski, C. R., Ramjist, J., da Costa, L., Black, S. E., and Yang, V. (2019). Optical coherence tomography imaging after endovascular thrombectomy for basilar artery occlusion: Report of 3 cases. *J. Neurosurg.* 2019, 1–6. doi:10.3171/2019.5.JNS191252

Ploner, S. B., Moult, E. M., Choi, W., Waheed, N. K., Lee, B., Novais, E. A., et al. (2016). Toward quantitative optical coherence tomography angiography: Visualizing blood flow speeds in ocular pathology using variable interscan time analysis. *Retina Phila. Pa.)* 36 (1), S118–s126. doi:10.1097/iae.0000000000001328

Prati, F., Regar, E., Mintz, G. S., Arbustini, E., Di Mario, C., Jang, I. K., et al. (2010). Expert review document on methodology, terminology, and clinical applications of optical coherence tomography: Physical principles, methodology of image acquisition, and clinical application for assessment of coronary arteries and atherosclerosis. *Eur. heart J.* 31, 401–415. doi:10.1093/eurheartj/ehp433

Saboori, P., and Sadegh, A. (2015). Histology and morphology of the brain subarachnoid trabeculae. *Anat. Res. Int.* 2015, 1–9. doi:10.1155/2015/279814

Saboori, P. (2021). Subarachnoid space trabeculae architecture. *Clin. Anat.* 34, 40–50. doi:10.1002/ca.23635

Shlofmitz, E., Shlofmitz, R. A., Galougahi, K. K., Rahim, H. M., Virmani, R., Hill, J. M., et al. (2018). Algorithmic approach for optical coherence tomography-guided stent implantation during percutaneous coronary intervention. *Interv. Cardiol. Clin.* 7, 329–344. doi:10.1016/j.iccl.2018.03.001

Su, J., Mathews, M. D., Nwagwu, C. I., Edris, A., Nguyen, B. V., Heidari, M., et al. (2008). Imaging treated brain aneurysms *in vivo* using optical coherence tomography. *Proc. SPIE* 6847, 684732.

Tearney, G. J., Brezinski, M. E., Bouma, B. E., Boppart, S. A., Pitris, C., Southern, J. F., et al. (1997). *In vivo* endoscopic optical biopsy with optical coherence tomography. *Science* 276, 2037–2039. doi:10.1126/science.276.5321.2037

Tearney, G. J., Regar, E., Akasaka, T., Adriaenssens, T., Barlis, P., Bezerra, H. G., et al. (2012). Consensus standards for acquisition, measurement, and reporting of intravascular optical coherence tomography studies: A report from the international working group for intravascular optical coherence tomography standardization and validation. *J. Am. Coll. Cardiol.* 59, 1058–1072. doi:10.1016/j.jacc.2011.09.079

Ughi, G. J., Marosfoi, M. G., King, R. M., Caroff, J., Peterson, L. M., Duncan, B. H., et al. (2020). A neurovascular high-frequency optical coherence tomography system enables *in situ* cerebrovascular volumetric microscopy. *Nat. Commun.* 11, 3851. doi:10.1038/s41467-020-17702-7

Ughi, G. J., Van Dyck, C. J., Adriaenssens, T., Hoymans, V. Y., Sinnaeve, P., Timmermans, J. P., et al. (2014). Automatic assessment of stent neointimal coverage by intravascular optical coherence tomography. *Eur. Heart J. - Cardiovasc. Imaging* 15, 195–200. doi:10.1093/ehjci/jet134

Ughi, G. J., Wang, H., Gerbaud, E., Gardecki, J. A., Fard, A. M., Hamidi, E., et al. (2016). Clinical characterization of coronary atherosclerosis with dual-modality oct and near-infrared autofluorescence imaging. *JACC Cardiovasc. Imaging* 9, 1304–1314. doi:10.1016/j.jcmg.2015.11.020

Van Gulick, L., Saby, C., Morjani, H., and Beljebbar, A. (2019). Age-related changes in molecular organization of type i collagen in tendon as probed by polarized shg and Raman microspectroscopy. *Sci. Rep.* 9, 7280. doi:10.1038/s41598-019-43636-2

Vardar, Z., King, R. M., Kraitem, A., Langan, E. T., Peterson, L. M., Duncan, B. H., et al. (2020). High-resolution image-guided web aneurysm embolization by high-frequency optical coherence tomography. *J. Neurointerv. Surg.* 13, 669–673. doi:10.1136/neurintsurg-2020-016447

Weigand, S., Saalfeld, S., Hoffmann, T., Eppler, E., Kalinski, T., Jachau, K., et al. (2019). Suitability of intravascular imaging for assessment of cerebrovascular diseases. *Neuroradiology* 61, 1093–1101. doi:10.1007/s00234-019-02233-w

Xu, C., Schmitt, J. M., Carlier, S. G., and Virmani, R. (2008). Characterization of atherosclerosis plaques by measuring both backscattering and attenuation coefficients in optical coherence tomography. *J. Biomed. Opt.* 13, 034003. doi:10.1117/1.2927464

Xu, X., Li, M., Liu, R., Yin, Q., Shi, X., Wang, F., et al. (2020). Optical coherence tomography evaluation of vertebrobasilar artery stenosis: Case series and literature review. *J. Neurointerv. Surg.* 12, 809–813. doi:10.1136/neurintsurg-2019-015660